

Signatures of microstreaming patterns induced by non-spherically oscillating bubbles^{a)}

Gabriel Regnault,^{1,b)} Cyril Mauger,^{1,c)} Philippe Blanc-Benon,¹ Alexander A. Doinikov,² and Claude Inserra³

¹Univ Lyon, École Centrale de Lyon, CNRS, Univ Claude Bernard Lyon 1, INSA Lyon, LMFA, UMR5509, 69130, F-69134 Écully, France

²Univ Lyon, École Centrale de Lyon, Collegium de Lyon, CNRS, Univ Claude Bernard Lyon 1, INSA Lyon, LMFA, UMR5509, 69130, Écully, France

³Univ Lyon, Université Lyon 1, Centre Léon Bérard, INSERM, LabTAU, F-69003, LYON, France

ABSTRACT:

In this study, we report recent theoretical and experimental developments dealing with the axisymmetric flow surrounding non-spherically oscillating microbubbles. A wide variety of microstreaming patterns is revealed using a theoretical modeling providing exact analytical solutions of the second-order mean flows. The streaming pattern is highly dependent on the modal content of the bubble interface oscillation, including possibly spherical, translational, and nonspherical modes, as well as any combination of these modes. Experimental results on fluid flow induced by a single, non-spherically oscillating bubble in an unbounded fluid are presented and successfully compared to the theoretical predictions. © 2021 Acoustical Society of America. <https://doi.org/10.1121/10.0005821>

(Received 22 January 2021; revised 13 July 2021; accepted 14 July 2021; published online 17 August 2021)

[Editor: James Friend]

Pages: 1188–1197

I. INTRODUCTION

Spherical, translational, and nonspherical bubble dynamics are significant phenomena in themselves, which are coupled in a nonlinear way at the timescale of the acoustic driving.^{1,2} Many studies have been devoted to the impact of the interaction of spherical and translational oscillations on the bubble motion^{3,4} or the organization of bubble clouds.⁵ The triggering of nonspherical modes through the process of parametric instability was mainly considered theoretically.^{2,6,7} Experimental investigations of nonspherical bubble oscillations have been performed on free gas bubble or ultrasound contrast agents, and allowed capturing some of the complex nonlinear phenomena arising when a bubble interface deviates from sphericity. This includes bubble coalescence⁸ or fragmentation processes,⁹ nonlinear coupling between nonspherical modes,¹⁰ or the influence of a nearby wall.¹¹ Another interesting feature resulting from bubble shape oscillations is the ability to generate steady circulation in the fluid near the vibrating bubble interface.¹² This circulation, whose explanation lies in the nonlinearity of the fluid dynamical equations, is usually called cavitation microstreaming. This fluid flow is slow in comparison to the acoustic timescale (the one of the bubble interface motion). Along with this mean flow come shear stresses and constraints in the presence of boundaries, as well as bubble self-

propulsion.¹³ Even if the steady stress may not be really large, it may serve as a continuous effect promoting the removal of surface-attached particles,¹⁴ the permeabilization of biological cell membranes,¹⁵ or the manipulation of living organisms.¹⁶

The physical origin of acoustic microstreaming is the interaction between at least two modes of the bubble oscillations. These modes include the breathing (purely spherical) mode, the bubble center translational mode or any nonspherical mode occurring along the bubble contour. Nyborg¹⁷ demonstrates that this coupling generates a second-order flow in the thin viscous layer surrounding the bubble, which then extends to the outer medium through viscous effects. Early theoretical studies were devoted to the analysis of microstreaming flows induced by the combination of spherical oscillations and the translation mode only,¹⁸ as this situation is likely to occur when a bubble oscillates near a wall. Later, the interactions between spherical and nonspherical oscillations¹³ or self-interaction of a single parametric shape mode¹⁹ have revealed a wide variety of streaming patterns that may arise when considering shape oscillations. All the above-mentioned theoretical works are based on the same approximation method that assumes a small viscous penetration depth in comparison to the bubble radius. This assumption limits the theoretical findings to the case of large bubbles or low-viscosity fluids. Recently, these limitations have been overcome in a theoretical modeling that includes all possible interactions between axisymmetric shape modes (including the spherical and translational ones) and provides exact solutions to the second-order mean flow.^{20–23}

^{a)}This paper is part of a special issue on Theory and Applications of Acoustofluids.

^{b)}Electronic mail: gabriel.regnault@insa-lyon.fr, ORCID: 0000-0002-7977-8549.

^{c)}ORCID: 0000-0001-7902-6075.

From an experimental point of view, microstreaming has been mostly investigated in the case of substrate-attached bubbles.^{24,25} The positional stability of the bubble is therefore ensured, hence facilitating the observation of the bubble-induced microstreaming. Maintaining the spatial stability of the bubble is crucial when studying microstreaming as it is a phenomenon occurring at a timescale that is much smaller than the characteristic time of the bubble oscillations. Microstreaming therefore requires a sufficient time to settle. However, the analysis of the interface dynamics of a wall-attached bubble is made complicated by the physics of the contact line dynamics,²⁶ or the triggering of asymmetric shape modes.²⁷ According to this, the analysis of microstreaming is usually not correlated to the bubble interface dynamics and consists of fairly qualitative observations. This drawback was recently raised using an acoustic levitation chamber,²⁸ in which a single trapped, non-spherically oscillating bubble, was kept stable for several minutes. Such a levitation system is commonly used when studying volume or shape oscillations of acoustically trapped bubbles or drop.^{29,30} This experimental setup allowed the quasi-simultaneous investigation of bubble nonspherical dynamics and induced microstreaming. A remarkable result was the capture of a large variety of microstreaming patterns induced by shape modes with order $n = 2, 3,$ or 4 . Surprisingly, various streaming patterns were obtained even when they were associated with an identical predominant shape mode. This feature was illustrated by the modification of the pattern shape for a bubble passing through the resonance size of a given shape mode. The origin of this modification was discussed along the change of phase shift between modes and the existence of secondary shape modes, but the exact cause of pattern evolution remained unclear.

In this work, we reveal the link between the bubble interface dynamics and the obtained liquid flows. In Sec. II, the theoretical modeling of the microstreaming induced by a bubble undergoing arbitrary axisymmetric shape oscillations is described theoretically and numerically. In Sec. III, the experimental setup allowing the measurement of both the bubble interface dynamics and the induced microstreaming is presented. In Sec. IV, experimental microstreaming patterns are compared to the theoretical model. The temporal evolution of microstreaming patterns is discussed in the case when the bubble size evolves from below to above the resonance size of a surface mode, or inversely. The importance of controlling the bubble interface dynamics for ensuring time-stable microstreaming is discussed in Sec. V.

II. THEORETICAL APPROACH

A. Microstreaming induced by a bubble undergoing axisymmetric shape oscillations

The system under study is a single gas bubble in an unbounded fluid. This bubble is driven by a uniform acoustic field, and its interface can undergo either spherical oscillations, a translational motion, or non-spherical deformations, as well as any combination of all of these modes.

These oscillation modes are, respectively, referred to as the zero-th order, the first order, and the n -order shape modes. Many theoretical works on nonspherical bubble dynamics have limited the mathematical derivation to the case of axisymmetric shape modes,^{13,19} an assumption that agrees with several experimental observations.³¹ Shape modes are known to be parametrically excited by the acoustically driven spherical oscillations of the bubble.⁶ Therefore, the predominant shape mode oscillates at half the driving frequency when triggered at its first parametric resonance. Several modes can coexist when being parametrically excited under the same acoustic conditions. In addition, when the onset of nonspherical oscillations is reached for a unique mode, several secondary shape modes can be excited at different angular frequencies through the process of nonlinear mode coupling.² As a consequence, the prediction of the modal decomposition of the bubble interface is not straightforward and contains many surfaces instabilities that evolve with different angular frequencies. According to this, the bubble surface $r_s(\theta, t)$ is expressed by

$$r_s(\theta, t) = R_0 + \sum_{n=0}^N a_n e^{-i\omega_n t} P_n(\cos \theta), \quad (1)$$

where R_0 is the radius at rest, a_n and ω_n are respectively the amplitude and the angular frequency of the n -th mode, N is the number of considered axisymmetric modes, and θ refers to the polar angle of the spherical system of coordinates (r, θ, ϕ) whose origin is at the bubble center. The hypothesis of axisymmetry allows one to disregard the ϕ -dependence in the problem. The function P_n refers to the Legendre polynomial of degree n that corresponds to the axisymmetric reduction of any spherical harmonics. In the modeling, the modal amplitudes a_n are supposed to be known and serve as input data for the theory. In comparison to previous theoretical works of Longuet-Higgins,¹⁸ Spelman and Lauga,¹³ or Maksimov,¹⁹ the present modeling does not consider the concept of viscous boundary layer whose interest lies in the splitting of the fluid domain surrounding the bubble into two regions where different simplified models of fluid motion can be applied. In the present mathematical derivation, we solve the equations of fluid motion all at once in the fluid domain surrounding the bubble. The only constraint on the shape mode amplitude is their smallness in comparison to the bubble radius, i.e., $\|a_n\|/R_0 \ll 1$. As a consequence, it is not important in our theory if the oscillation amplitudes of the radial or shape modes are larger than the boundary layer thickness.

It is first required to calculate the first-order liquid velocity v_1 by solving the linearized Navier-Stokes equations of an incompressible viscous unbounded liquid. The existence of the bubble interface imposes boundary conditions that are (i) the equality between the normal component of v_1 at the interface $r = R_0$ and the normal component of the velocity of the bubble wall and (ii) the condition of slip-page on the gas-liquid interface for an uncoated bubble, such that the tangential stress vanishes on the bubble

surface. If one assumes that the bubble interface contains a pair of modes n and m , hence the velocity field is written as

$$\mathbf{v}_1 = \mathbf{v}_{1n} + \mathbf{v}_{1m}, \quad m \neq n. \quad (2)$$

From a mathematical point of view, acoustic streaming is a second-order, time-averaged effect. The streaming velocity field $\mathbf{v}_2 = \nabla \times \psi_2$ is therefore derived by solving the nonlinear incompressible Navier-Stokes equations up to the second-order terms with respect to the linear solutions. Here, only the vortical part of the velocity field is kept in order to describe the recirculation vortices.¹⁸ After averaging over time, the streaming vector potential is obtained by solving

$$\Delta^2 \langle \psi_2 \rangle = -\frac{1}{\nu} \nabla \times \langle \mathbf{v}_1 \cdot \nabla \mathbf{v}_1 \rangle, \quad (3)$$

where ν is the kinematic liquid viscosity and $\langle \rangle$ denotes the time average. In view of the time-averaging process in Eq. (3), nonzero contributions to acoustic streaming can come either from pairs of modes that oscillate at the same frequency $\omega_n = \omega_m$, or from the interaction of a mode with itself.²⁰ Therefore, the vector potential ψ_2 that characterizes the Eulerian streaming can be split into three parts

$$\langle \psi_2 \rangle = \langle \psi_2^{nn} \rangle + \langle \psi_2^{mm} \rangle + \langle \psi_2^{nm} \rangle, \quad (4)$$

where $\langle \psi_2^{nm} \rangle$ is produced by the interaction of modes n and m and $\langle \psi_2^{nn} \rangle$ is produced by mode n alone, and equivalently for $\langle \psi_2^{mm} \rangle$. In the process of deriving the streaming velocity \mathbf{v}_2 , boundary conditions are applied: (i) zero streaming velocity is imposed at infinity and (ii) normal velocity components and tangential stress of the Lagrangian streaming must vanish at the mean position of the bubble interface. To calculate the Lagrangian velocity, it is required to derive the Stokes drift velocity \mathbf{v}_S , such that the Lagrangian streaming velocity \mathbf{v}_L is

$$\mathbf{v}_L = \mathbf{v}_2 + \mathbf{v}_S. \quad (5)$$

Due to the multiple components existing into the vector potential in Eq. (4), a wide variety of streaming patterns arise from different mode interactions. When considering the interaction between the spherical mode and any shape mode oscillating at the driving frequency, meaningly the $0 - n$ interaction,²⁰ the streaming pattern looks like a lobe-type pattern whose lobes number equals $2n$. When the bubble translation interacts with any nonspherical mode n ,²¹ streamlines form lobes whose number is equal to $2(n - 1)$. In the self-interacting case,²² a two-scale streaming field appears with lobes in the near-field of the bubble interface, while the far-field pattern exhibits a cross-like shape. When mode $n > m$ interacts with mode $m \geq 1$,²³ $2|n - m|$ lobes arise in the far field. A MATLAB code for the calculation of the Eulerian, Stokes drift, and Lagrangian velocity fields, as well as the computation of the streamlines, is provided.³² The variety of streaming patterns is illustrated in Fig. 1 for $(n, m) \in [0, 1, 2, 3, 4, 5]^2$. The calculations are performed for

a bubble in water, whose radius is $R_0 = 50 \mu\text{m}$, and for modes oscillating at $f = 30 \text{ kHz}$. The phase shift between the modes is set to $\Delta_\phi^{n-m} = \pi/4$, if $n \neq m$. The left lower part illustrates the deformation of the bubble interface for the considered (n, m) pair of modes. In mirror to the diagonal $n = m$, the right upper part provides the corresponding streaming pattern. The diagonal contains streamlines coming from the self-interacting case. The higher the mode number, the higher the possibility of lobe-type patterns. In addition, the higher the mode number, the higher the number of mode interactions that arise because of nonlinear coupling. This makes the prediction of the resulting flow pattern particularly complex.

B. Numerical prediction of bubble-induced microstreaming

When subject to a locally uniform ultrasound wave, a gas bubble exhibits nonspherical deformations if it is excited above a given pressure threshold.⁶ As the equations governing the shape mode oscillations are nonlinearly coupled, a rich modal spectrum may arise on the bubble surface. To depict the resulting microstreaming pattern, we compute the steady-state amplitudes of axisymmetric shape modes by using the mathematical formulation of Shaw.² This model is accurate up to the second order of the small parameter $\epsilon = a_n/a_0 \ll 1$. Good agreement was previously evidenced between this modeling and experimental investigations of nonspherical bubble dynamics.^{8,10} Simulations of the temporal evolution of the bubble interface are performed with the following initial conditions: $R(0) = R_0$ and $a_i(0) = 0.1 \mu\text{m}$. A harmonic driving field is considered, $p(t) = P_{ac} \sin(\omega_{ac}t)$, where P_{ac} is the acoustic amplitude and ω_{ac} is the angular frequency. Figure 2 provides the evolution of shape mode amplitudes over two acoustic periods, their spectral analysis and the resulting fluid flow pattern in the case of a bubble of equilibrium radius $R_0 = 45 \mu\text{m}$ driven at the pressure amplitude $P_{ac} = 20 \text{ kPa}$. Such forcing conditions allows one to trigger the shape mode 2 at its first parametric resonance. Figure 2(a) describes the rich modal content of the bubble interface motion resulting from nonlinear coupling. The most unstable mode ($n = 2$) reaches the largest amplitude $a_2 \sim 6 \mu\text{m}$ and oscillates at half the driving frequency. Due to mode coupling, the even shape modes $n = 4, 6, 8$ are excited. Considering their small amplitudes, modes 6 and 8 are disregarded in the following. It is worth noting that mode 4 oscillates at the driving frequency, with the phase shift $\Delta_\phi^{0-4} = 0.89 \text{ rad}$ with respect to the radial mode. The spectrum of the interface motion is summarized in Fig. 2(b), where the mode amplitudes are plotted as a function of the angular frequency. For each oscillation mode, its nonlinear behavior is disregarded in the calculation of the resulting microstreaming. This means that the main frequency component of each shape mode is only kept in the following. We remind that microstreaming comes only from the interaction of modes oscillating at the same angular frequency or through self-interacting modes. Therefore, the fluid flow is described by the Lagrangian velocity

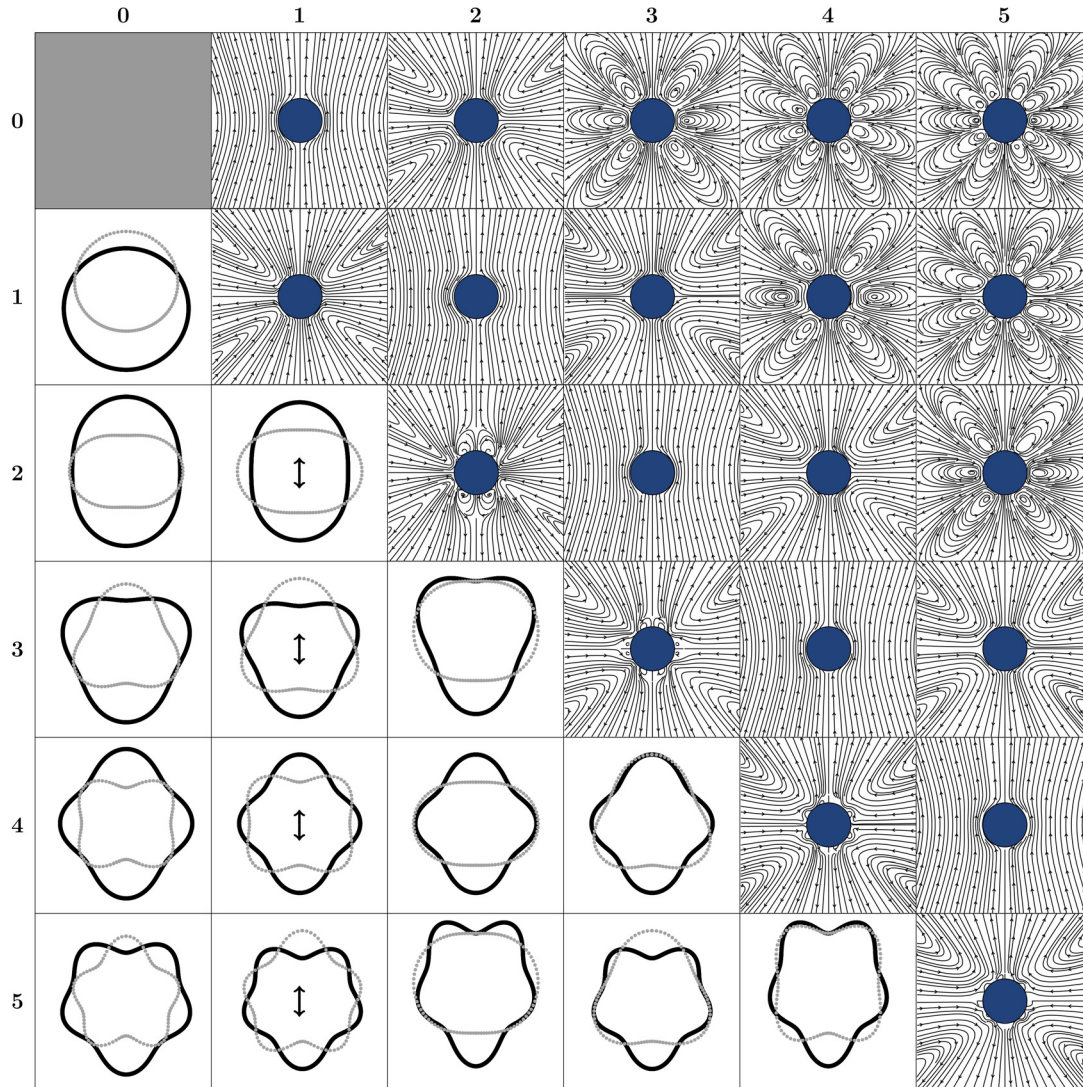


FIG. 1. (Color online) Microstreaming patterns generated by different mode interactions. The right upper part displays the streaming pattern predicted for interactions between mode m ($0 \leq m \leq 5$) and mode n ($0 \leq n \leq 5$). Mirror to the diagonal $n = m$, the corresponding bubble shape deformation is displayed. The diagonal contains streaming patterns coming from the self-interaction of an axisymmetric mode.

$$v_L = v_L^{0-4}(\omega_{ac}) + v_L^{4-4}(\omega_{ac}) + v_L^{2-2}(\omega_{ac}/2). \quad (6)$$

The resulting streaming pattern as well as the ones induced by every modal interaction appearing in Eq. (6) are displayed in Fig. 2(d). The overall streaming flow is governed mainly by the 2 – 2 interaction that consists in a long range, cross-like pattern with four lobes confined nearby the bubble interface. In comparison with the case 2 – 2 alone, a slight decrease in the radial extension of the lobes is observed. This effect is explained when considering the contribution coming from the interaction 0 – 4. In order to illustrate the relative weight of each interaction in the overall pattern, Fig. 2(c) shows the average value of the Lagrangian velocity $\|v_L^{n-m}\|$ on a circle surrounding the bubble center as a function of the normalized distance r/R_0 for the three predominant interactions. The interaction 2 – 2 dominates, but the one coming from the interaction 0 – 4 cannot be neglected, particularly close to the bubble

interface [see inset of Fig. 2(c)]. This is partly due to the high value of the phase shift between modes 0 and 4.

In Sec. IV, experimental streaming patterns will be investigated in a similar way. In addition, analysis of the bubble interface motion will serve as input data for the theoretical modeling and allow numerical comparison of the microstreaming patterns.

III. EXPERIMENTAL APPROACH

The experimental setup and methods were already described in detail in a previous study.²⁸ Therefore, we describe shortly the acoustic levitation chamber, the mode triggering by a coalescence technique, and measurements of fluid flows. Figure 3 depicts the experimental setup allowing the nucleation and trapping of gas microbubbles, before capturing quasi-simultaneously (i) their nonspherical oscillations [Fig. 3(a)] and (ii) the induced fluid flow [Fig. 3(b)].

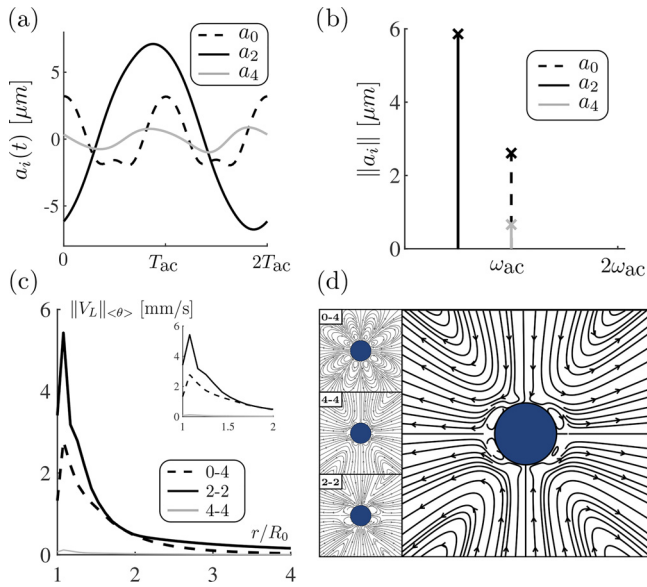


FIG. 2. (Color online) Microstreaming predictions in the case of a $45 \mu\text{m}$ bubble excited by a 31.25 kHz ultrasound field of amplitude 20 kPa . The bubble interface motion is obtained from the model of Shaw (Ref. 2). (a) Temporal oscillations of the predominant shape modes over two acoustic periods. (b) Fourier analysis of the shape modes. (c) Radial evolution of the velocity profile for every predominant interaction $m-n$. $\|V_L\|_{\langle\theta\rangle}$ is the norm of the Lagrangian velocity averaged along a circle of radius r/R_0 . A closer look at the velocity near the bubble interface is provided in the insert. (d) Overall streaming pattern resulting from the summation of the considered interactions.

A. The acoustic levitation chamber

A 8 cm -edge cubic tank is filled with filtered water (Carlo Erba, Water for analysis). Single bubbles are nucleated by short laser pulses using a Nd: YAG pulsed laser ($\lambda = 532 \text{ nm}$ NewWave Solo PIVIII), focused through a lens-set. In general, every laser pulse leads to the generation of a single bubble with a radius ranging from 20 to $50 \mu\text{m}$. A 31.25 kHz standing wave is set inside the tank using a Langevin (SinapTec[®], 31 kHz resonance frequency) transducer. The driving frequency corresponds to one acoustic mode of the

cavity. Care has been taken to consider a resonance mode containing at least one pressure antinode inside the tank, at which the bubble will be trapped as it is smaller than the resonant size $R_{\text{res}} \simeq 110 \mu\text{m}$. Being positionally stable at the pressure antinode, the bubble experiences spherical oscillations in the driving field. The dynamics of the bubble interface is recorded using a CMOS camera (Vision Research[®], V12.1, 180 kfps frame rate at 128×128 pixel size) equipped with a $12\times$ objective lens (Navitar[®] with an additional $1.5\times$ lens).

B. Triggering of bubble nonspherical oscillations

A coalescence technique⁸ is used in order to trigger bubble nonspherical oscillations. This technique has demonstrated efficiency for the induction of steady-state, symmetry-controlled, shape modes. A first bubble is laser-nucleated and trapped at the pressure antinode. The driving pressure amplitude is chosen in such a way that this bubble exhibits only radial oscillations. Then, a second bubble is nucleated and moves towards the same pressure antinode, where the first one is already trapped. When reaching the trapping location, the two bubbles attract each other and merge into a single one. Nonspherical oscillations are triggered if the coalesced bubble size and the applied acoustic pressure fulfill the conditions for shape mode excitation. If not, multiple coalescences are performed following the same procedure. It has been shown that the symmetry axis of the shape mode corresponds to the approaching axis of the two coalescing bubbles. If the rectilinear motion of the coalescing bubbles belongs to the focal plane of the camera, then the axisymmetric shape modes are perfectly defined from a two-dimensional recording. Therefore, the bubble interface can be decomposed into the set of Legendre polynomials

$$r(\theta, t) = \sum_{n=0}^{\infty} a_n(t) P_n(\cos \theta), \tag{7}$$

where the modal coefficients $a_n(t)$ are extracted from the orthogonality relationship

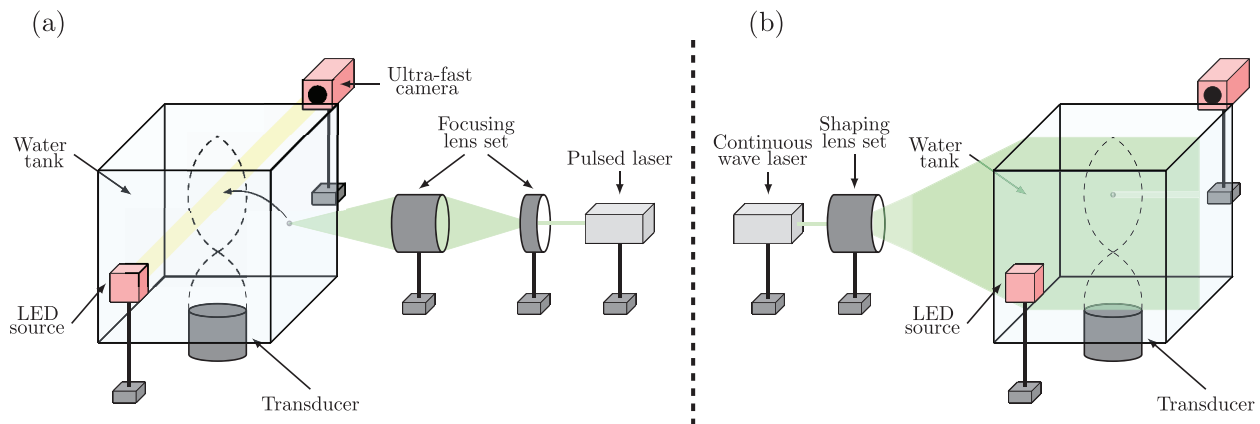


FIG. 3. (Color online) Schematics of the experimental set-up used to capture both the temporal dynamics of a bubble and its associated microstreaming. (a) The bubble is created using a focused pulsed-laser and then trapped at an antinode of a 31.25 kHz standing wave. The oscillations are recorded with a high frame rate camera (180 kfps). (b) A thin laser sheet (about $150 \mu\text{m}$ in depth) lights the focal plane of the camera. Micrometric fluorescent markers are mixed in the fluid and allows following the fluid motion. Their motion is recorded at a lower frame rate (600 fps).

$$a_n(t) = \frac{2n+1}{2} \int_{-1}^1 r(x,t) P_n(x) dx, \quad x = \cos \theta. \quad (8)$$

C. Measurement of bubble-induced microstreaming

The fluid flow generated around the oscillating bubble is visualized using fluorescent tracers (R700 ThermoFisher, diameter 0.71 μm) injected inside the tank. The particles are illuminated by a continuous wave laser (CNI 400 mW, 532 nm) coupled to a cylindrical lens in order to form a thin laser sheet (thickness 150 μm). Care has been taken to choose fluorescent particles that are able to follow accurately the fluid flows (Stokes number ≪ 1) and small enough so that they are not subjected to primary radiation force.³³ The motion of the particles is captured with an acquisition rate of 600 Hz, frame size 1024 × 768 pixels. The laser sheet is adjusted to match the focal plane of the camera. This experimental set-up is depicted in Fig. 3(b).

In order to assess quasi-simultaneously both the bubble interface dynamics and the induced fluid flow, recordings of acoustofluidic phenomena acting on the fast (180 kHz frame rate) and slow (600 Hz) timescale are alternately performed. Two consecutive identical recordings of the bubble interface ensure the stability of the bubble dynamics during the fluid flow measurement. The obtained microstreaming is hence confidently correlated to the measured bubble dynamics.

The motion of the particles is post-processed in two ways. The first one consists in superimposing all the snapshots of the recording by keeping the maximum value of every pixel. This leads to a streak imaging of the streaming pattern. The second one consists of a particle tracking velocimetry (PTV) analysis of the flow. The particle displacement between every frame is analyzed using the Trackmate tool³⁴ on the IMAGEJ software. Their trajectories allow quantifying the velocity field in the Lagrangian formalism.

IV. EXPERIMENTAL RESULTS

A large variety of microstreaming flows has already been reported by Cleve *et al.*²⁸ In the following, we first compare experimental flows to those obtained by the modeling^{20–23} before analysing the resulting velocity field. Second, we demonstrate that the theoretical work allows retrieving the modification of the patterns structure for a bubble passing through the shape resonance size.

A. Analysis of the microstreaming pattern

Following the procedure detailed in Sec. II B, experimental microstreaming flows are compared to theoretical predictions.

Experimental and theoretical results are compared in Figs. 4(a)–4(c) for a bubble of radius $R_0 = 65 \mu\text{m}$ driven at

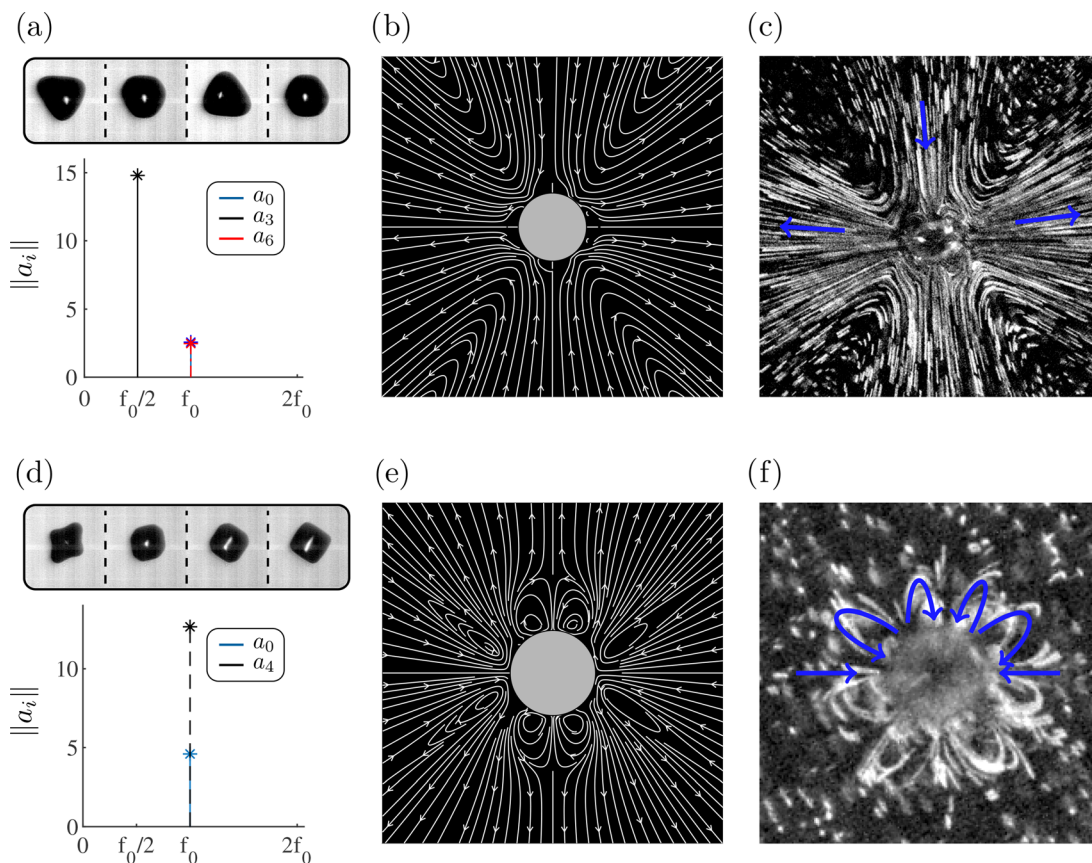


FIG. 4. (Color online) Comparison between experimental and theoretical microstreaming patterns for bubbles oscillating on the predominant mode 3 (a)–(c) or 4 (d)–(f). (a), (d) Snapshot series of the bubble interface and spectrum of the predominant shape oscillations. (b), (e) The predicted microstreaming pattern, and (c), (f) the experimental one.

the acoustic pressure $P_{ac} = 9$ kPa. The dynamics of the bubble interface and its modal decomposition [Fig. 4(a)] reveal that this bubble exhibits predominantly the shape mode with $n = 3$ excited at its first parametric resonance. Due to nonlinear coupling, a secondary shape mode $n = 6$ is triggered with a significantly smaller oscillation amplitude. The computed theoretical flow is shown in Fig. 4(b). This pattern matches successfully with the experimental one, provided in Fig. 4(c). It consists of a large-scale cross with four recirculation vortices regularly distributed around the bubble interface. Both shape and radial extensions of the vortices are in good agreement. The direction of velocity along streamlines is also recovered by the theoretical modelling. The results indicate that the main modal interaction contributing to the overall pattern is the 3 – 3 interaction (see Fig. 1).

The second case is a bubble of equilibrium radius $R_0 = 54 \mu\text{m}$ driven at the acoustic pressure $P_{ac} = 25$ kPa. Snapshot series of the bubble contour reveal the predominant mode 4 that is triggered at its second parametric resonance, hence oscillating at the driving frequency [Fig. 4(d)]. Only the 0–4 interaction and the self-interaction 4–4 contribute to the streaming flow, and the streaming velocity is described by

$$v_L = v_L^{0-4}(\omega_{ac}) + v_L^{4-4}(\omega_{ac}). \quad (9)$$

The predicted streaming pattern is displayed in Fig. 4(e). A lobe-type pattern is obtained, consisting of eight lobes regularly distributed around the bubble. A fairly good agreement is obtained with the experimental results shown in Fig. 4(f). In this case, the dominating contribution to the streaming flow is the cross-interaction 0–4. Videos of the bubble oscillations and induced fluid-flow, for the two above-mentioned cases are provided in Mm. 1, Mm. 2, Mm. 3, and Mm. 4.

Mm. 1. High-speed recording of the bubble shown in Fig. 4(a). The bubble oscillates on a main mode 3. This is a file of type “mov” (584 KB).

Mm. 2. Flow induced by the bubble shown in MM. 1. This is a file of type “mov” (61.4 MB).

Mm. 3. High-speed recording of the bubble shown in Fig. 4(d). The bubble oscillates on a main mode 4. This is a file of type “mov” (451 KB).

Mm. 4. Flow induced by the bubble shown in MM. 3. This is a file of type “mov” (32 MB).

B. Evolution of the microstreaming velocity

PTV analysis of the flow has been performed for the two experimental cases presented in Sec. IV A. Figure 5 shows experimental and theoretical values of the magnitude of the Lagrangian velocity along the axis $\theta = 0$ (corresponding to the horizontal line passing through the bubble center in Fig. 4(b), for instance). Figure 5(a) corresponds to the case of the predominant mode 3 while Fig. 5(b) accounts for mode 4. Lagrangian velocities are plotted as a function of the normalized distance r/R_0 in a log-log representation. In

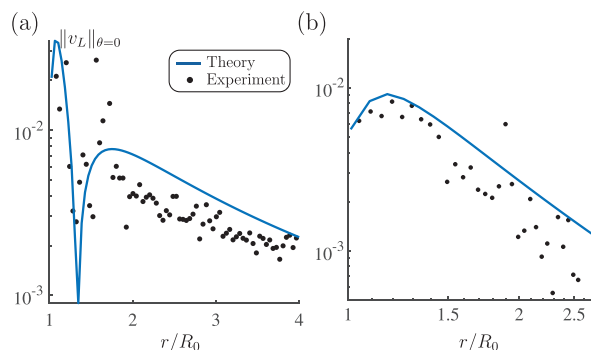


FIG. 5. (Color online) Evolution of the amplitude of the Lagrangian velocity along the axis $\theta = 0$ as a function of the normalized distance r/R_0 . Theoretical (solid line) and experimental (dots) results are displayed in a log-log scale for (a) the case of the predominant mode 3 and (b) the predominant mode 4.

Fig. 5(a), the amplitudes are well recovered, while in Fig. 5(b), the theoretical prediction has been adjusted in order to match the experimental amplitudes. As pointed out in Fig. 5, a good agreement is obtained between the velocity profiles. If the measured experimental values of shape mode amplitudes and phase delay are injected in the numerical simulations, then the velocity amplitude is quantitatively recovered in Fig. 5(a) (for $n = 3$), but is overestimated by a factor of 5 in Fig. 5(b) (for $n = 4$). For this last case, experimental streaming velocities reach 1.5 mm/s at the distance $2R_0$ from the bubble interface while the value of ~ 7 mm/s is theoretically predicted. Such a discrepancy can be explained by several experimental limitations. From an experimental point of view, the accurate measurement of the Lagrangian streaming velocity cannot be ensured, particularly in the vicinity of the bubble interface. Indeed, next to the bubble interface, the flow-tracking particles are subjected to drag forces and to secondary Bjerknes forces that are not negligible. In addition, theoretical streaming velocities are scaled quadratically with the shape mode amplitudes. As a consequence, an overestimation of the parameters resulting from the modal decomposition (mode amplitude, phase delay) of the bubble interface motion can lead to an overestimation of the predicted streaming velocity amplitude. Therefore, at this stage, we limit our analysis to the radial evolution of the streaming velocity amplitude. A more quantitative investigation that considers all the above-mentioned experimental restrictions will be the object of further considerations.

C. Temporal evolution of the microstreaming pattern

Most of the conducted experiments concerned bubbles whose sizes were approximately stable over time, such that the resulting microstreaming flows were time-stable. However, in a few cases we have observed bubbles growing or shrinking over time. Shape oscillations have also been shown to fasten bubble growth by the enhancement of rectified diffusion.³⁵ In this case, the bubble size might change from above to below the resonance size of a surface mode, or inversely. One example is shown in Fig. 6. In that case, we managed to record the relatively fast switch between a

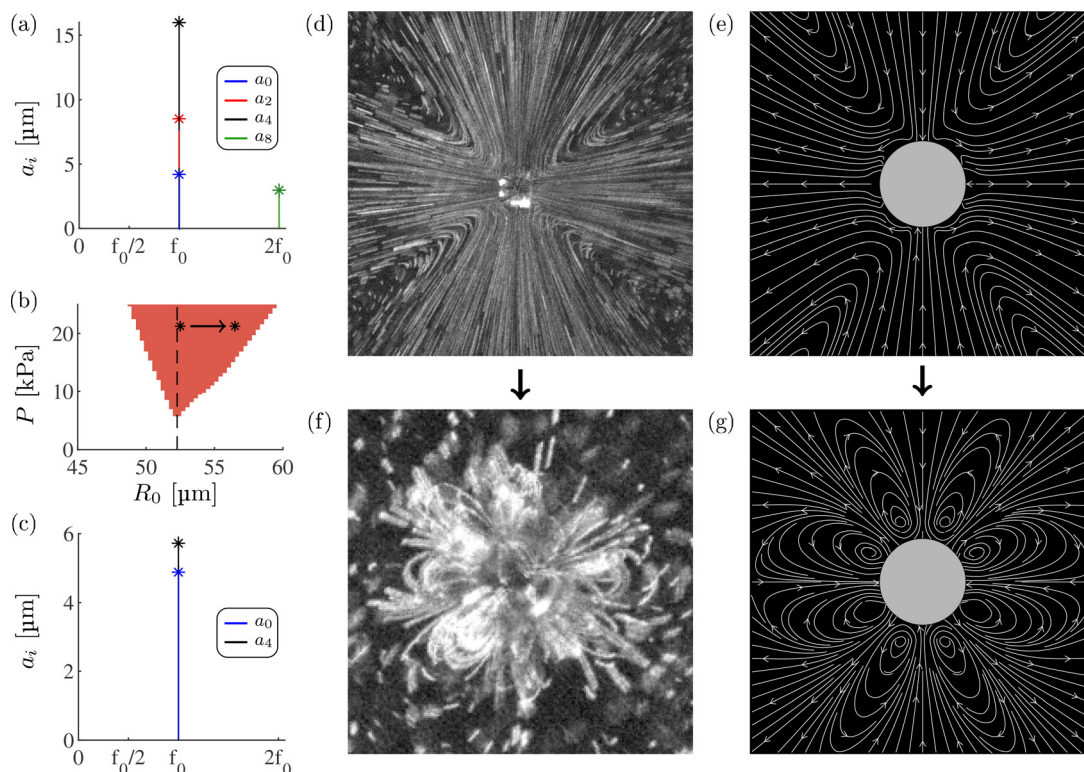


FIG. 6. (Color online) Evidence of streaming pattern evolution for a growing bubble, subject to an acoustic pressure of about 20 kPa, and oscillating on mode 4. (a) and (e) show the modal content of the bubble before and after the growth, respectively. The size evolution is depicted in (d), where the red zone corresponds to that of mode 4 triggered at the secondary parametric resonance (Ref. 6). When the bubble size is close to the resonance, the modal content is richer. The experimental fluid flow patterns obtained before and after the growth are shown in (b) and (f). Similarly, predicted patterns are shown in (c) and (g). A good agreement is found between experimental patterns and theoretically predicted ones.

cross-type pattern [Fig. 6(b)] to a lobe-type pattern [Fig. 6(f)]. The corresponding bubble dynamics before and after the recording of the streaming flow reveals a growth of the bubble size. Initially around the resonant radius $R \sim 52 \mu\text{m}$ of the surface mode 4, its size evolves to nearly $57 \mu\text{m}$, remaining in the instability zone of mode 4 [Fig. 6(d)]. When moving away from the resonance size, the modal content of the bubble interface motion significantly changes. Near the resonance of the surface mode, the interface motion exhibits several secondary modes (namely, modes 2 and 8) in addition to the predominant unstable mode 4 [oscillating at the driving frequency, see Fig. 6(a)]. Many modal interactions occur and lead to the predicted streaming pattern shown in Fig. 6(c) that coincides well with the experimental one. When moving away from the resonance size, the modal content restricts only to the radial oscillation and the unstable mode 4 [Fig. 6(e)]. In this case, the predicted pattern shown in Fig. 6(g) is a lobe-type pattern that only results from the 0–4 interaction. This pattern correctly describes the experimental one.

V. DISCUSSION

Most studies on acoustic microstreaming are performed with substrate-attached bubbles, so that the positional stability of the bubble is maintained. This configuration facilitates the observation of the induced flow surrounding the

bubble.^{25,36–38} However, the behavior and the interpretation of the bubble interface are more complex due to the symmetry breaking induced by the substrate. The contact of the bubble with a surface facilitates the triggering of asymmetric modes,²⁷ with fast transition to chaotic surface regimes.³⁹ Apart from the experimental convenience of using wall-attached bubbles, their study is fundamental in the context of therapeutic drug delivery applications in which oscillating microbubbles might be poked to the cell membrane.^{40,41} Even if they are not bound to the cell membrane, it is clear that microbubbles must be brought in the close vicinity of the target cells or vessels in order to induce a significant mechanical action on the surrounding living material. In this perspective, an alternative approach for the investigation of microbubble-induced effects can be performed in two stages: (i) the interface dynamics and induced flows are investigated in the case of a free microbubble (far from any boundary) and (ii) nearby spherical bodies (such as cells) or rigid or elastic walls (mimicking vessels or biological barriers) are appended. The advantages arising from this approach are twofold: nonspherical microbubble dynamics is well documented in the case of free bubbles exhibiting axisymmetric interface motion, both theoretically^{1,2} and experimentally,¹⁰ and theoretical studies on cavitation microstreaming only concern free bubbles.^{13,20} Still, even the axisymmetric oscillations of an acoustically driven bubble are a complicated matter due to nonlinear mode

coupling.¹⁰ Many nonspherical modes may exist simultaneously once an unstable parametric mode is triggered. Theoretical modeling of cavitation streaming has revealed that unique flow patterns are obtained depending on the interaction between two nonspherical modes (including the radial and the translational ones), as depicted in Fig. 1. The knowledge of the bubble interface dynamics is hence of primary importance in the understanding of streaming flows. For instance, a bubble oscillating on a predominant unstable mode triggered at its first parametric resonance induces a microstreaming dictated by the nonspherical mode self-interaction, as shown in Fig. 4(c) for the predominant mode 3. This pattern significantly differs from the one obtained in the case of an unstable mode triggered at its second parametric resonance. When the surface mode oscillates at the driving frequency and excites secondary shape modes, many interactions have to be considered for the determination of the flow pattern. A large variety of patterns arises (Fig. 1) with clear differentiation between cross-like and lobe-type patterns. The latter is obtained here in the case of the predominant mode 4, as shown in Fig. 4(f).

To confirm the importance of correlating the bubble interface dynamics and the induced flows, the case of a time-evolving streaming flow is depicted in Fig. 6. The transition of the bubble-induced flow took place during the recording, and evolved from a cross-like to a lobe-type pattern. Such transitions have already been observed for substrate-attached bubbles,^{25,42} but they were the result of variation of the shape mode order. Here, the predominant triggered mode remains the same over the duration of the recordings, as the bubble size evolves within the instability zone of a given surface mode [Fig. 6(d)]. The change of the streaming pattern is therefore only related to the modification of the bubble interface dynamics. When passing through the modal resonance frequency, phase inversion occurs for the nonspherical instability.⁴³ It is known that the intensity of the microstreaming strongly depends on the phase shift between two interacting modes,²⁰ and reaches a maximum when the phase shift equals $\pi/2$. It is worth noting that the intensity of microstreaming produced by the self-interacting shape mode only depends on the mode amplitude. As a consequence, the relative weight of several contributions participating in the streaming flow is modified when the bubble size evolves. We believe that these observations can have practical use in bubble-mediated medical and engineering applications. In therapeutic applications, bubbles are known to act as vectors for permeabilizing tight junctions between cells and the cell membrane itself.⁴⁴ In the case of stably oscillating microbubbles, such phenomena may occur due to the shear stress or shear stress gradients⁴⁵ acting on the biological membranes. Such stresses are induced by the generation of microstreaming flows around bubbles. In this context, differentiating large-scale or small-scale vortices in the vicinity of oscillating bubbles matters for a safe prediction of the mechanical action of bubbles in their vicinity. We point out that we have adapted here the spatiotemporal scale in the experimental studies with respect

to those used in therapeutics due to experimental limitation. The investigated bubbles are one or two orders of magnitude larger than the coated micrometric bubbles used in medical applications. However, a similar observation of shape modes triggering and dynamics were performed by Dollet *et al.*⁴⁶ on ultrasound contrast agent microbubbles: a shape mode $n = 4$ was triggered in a 1.7 MHz field at 200 kPa pressure amplitude. Therefore, after frequency and size scaling, it is reasonable to assume that the main features of bubble shape modes dynamics and resulting microstreaming are similar in the here-presented experiments and in the case of smaller bubbles. In engineering applications, bubbles are known to be a key mechanism underlying ultrasound-induced surface cleaning.¹⁴ Common ultrasonic techniques rely on the use of the inertial cavitation regime in which bubble collapses are favored in order to clean sub-micron particles from surfaces. These ultrasonic cleaning methods can be too severe for sensitive cleaning applications. The soft cavitation regime, such as stably oscillating microbubbles at the surface boundary, has been shown to be partly able to remove contamination particles under damage-free conditions.⁴⁷ We expect that a better understanding of the microstreaming phenomenon as well as its correlation to the microbubble dynamics will help in the improvement of such bubble-mediated techniques.

VI. CONCLUSION

In this work, we reported recent developments of theoretical and experimental analysis of bubble-induced microstreaming. Depending on the bubble dynamics, a large variety of microstreaming patterns is expected. Two classes of patterns appear: the cross-type (large scale) patterns and the sunflower-like (small scale) ones. The condition of appearance of one class of each class of pattern relies on the number and order of shape modes that develop on the bubble interface. For different predominant shape modes, this behavior is experimentally demonstrated and successfully compared to a theoretical modeling providing the exact solution of the second order liquid flow. These results suggest that a safe prediction of streaming flows requires a good control of the bubble size and dynamics of nonspherical oscillations over time.

ACKNOWLEDGMENTS

This work was supported by the LabEx CeLyA of the University of Lyon (Grant No. ANR-10-LABX-0060/ANR-11-IDEX-0007). The authors also thank the Collegium of Lyon for the support of A.A.D.

¹A. A. Doynikov, "Translational motion of a bubble undergoing shape oscillations," *J. Fluid Mech.* **501**, 1–24 (2004).

²S. J. Shaw, "Translation and oscillation of a bubble under axisymmetric deformation," *Phys. Fluids* **18**(7), 072104 (2006).

³C. Desjouis, P. Labelle, B. Gilles, J.-C. Bera, and C. Insera, "Orbital trajectory of an acoustic bubble in a cylindrical resonator," *Phys. Rev. E* **88**, 033006 (2013).

⁴R. Mettin and A. A. Doynikov, "Translational instability of a spherical bubble in a standing ultrasound wave," *Appl. Acoust.* **70**(10), 1330–1339 (2009).

- ⁵J. R. Blake, U. Parlitz, R. Mettin, S. Luther, I. Akhatov, M. Voss, and W. Lauterborn, "Spatiotemporal dynamics of acoustic cavitation bubble clouds," *Philos. Trans. R. Soc. London Ser. A* **357**(1751), 313–334 (1999).
- ⁶M. P. Brenner, D. Lohse, and T. F. Dupont, "Bubble shape oscillations and the onset of sonoluminescence," *Phys. Rev. Lett.* **75**, 954–957 (1995).
- ⁷S. J. Shaw, "The stability of a bubble in a weakly viscous liquid subject to an acoustic traveling wave," *Phys. Fluids* **21**(2), 022104 (2009).
- ⁸S. Cleve, M. Guédra, C. Inserra, C. Mauger, and P. Blanc-Benon, "Surface modes with controlled axisymmetry triggered by bubble coalescence in a high-amplitude acoustic field," *Phys. Rev. E* **98**, 033115 (2018).
- ⁹M. Postema, P. Marmottant, C. T. Lancée, S. Hilgenfeldt, and N. de Jong, "Ultrasound-induced microbubble coalescence," *Ultrasound Med. Biol.* **30**, 1337–1344 (2004).
- ¹⁰M. Guédra, C. Inserra, C. Mauger, and B. Gilles, "Experimental evidence of nonlinear mode coupling between spherical and nonspherical oscillations of microbubbles," *Phys. Rev. E* **94**, 053115 (2016).
- ¹¹V. Garbin, D. Cojoc, E. Ferrari, E. D. Fabrizio, M. L. J. Overvelde, S. M. van der Meer, N. de Jong, D. Lohse, and M. Versluis, "Changes in microbubble dynamics near a boundary revealed by combined optical micromanipulation and high-speed imaging," *Appl. Phys. Lett.* **90**(11), 114103 (2007).
- ¹²J. Kolb and W. L. Nyborg, "Small scale acoustic streaming in liquids," *J. Acoust. Soc. Am.* **28**(6), 1237–1242 (1956).
- ¹³T. Spelman and E. Lauga, "Arbitrary axisymmetric steady streaming: Flow, force and propulsion," *J. Eng. Math.* **105**, 31–65 (2017).
- ¹⁴F. Reuter and R. Mettin, "Mechanisms of single bubble cleaning," *Ultrasonics Sonochem.* **29**, 550–562 (2016).
- ¹⁵I. Lentacker, I. De Cock, R. Deckers, S. D. Smedt, and C. Moonen, "Understanding ultrasound induced sonoporation: Definitions and underlying mechanisms," *Adv. Drug Del. Rev.* **72**, 49–64 (2014).
- ¹⁶D. Ahmed, A. Ozcelik, N. Bojanala, N. Nama, A. Upadhyay, Y. Chen, W. Hanna-Rose, and T. Huang, "Rotational manipulation of single cells and organisms using acoustic waves," *Nat. Commun.* **7**, 11085 (2016).
- ¹⁷W. Nyborg, "Acoustic streaming," *Phys. Acoust.* **2**, 265–331 (1965).
- ¹⁸M. S. Longuet-Higgins, "Viscous streaming from an oscillating spherical bubble," *Proc. R. Soc. London Ser. A* **454**(1970), 725–742 (1998).
- ¹⁹A. Maksimov, "Viscous streaming from surface waves on the wall of acoustically-driven gas bubbles," *Euro. J. Mech. B/Fluids* **26**(1), 28–42 (2007).
- ²⁰A. A. Doinikov, S. Cleve, G. Regnault, C. Mauger, and C. Inserra, "Acoustic microstreaming produced by nonspherical oscillations of a gas bubble. I. Case of modes 0 and m," *Phys. Rev. E* **100**, 033104 (2019).
- ²¹A. A. Doinikov, S. Cleve, G. Regnault, C. Mauger, and C. Inserra, "Acoustic microstreaming produced by nonspherical oscillations of a gas bubble. II. Case of modes 1 and m," *Phys. Rev. E* **100**, 033105 (2019).
- ²²C. Inserra, G. Regnault, S. Cleve, C. Mauger, and A. A. Doinikov, "Acoustic microstreaming produced by nonspherical oscillations of a gas bubble. III. Case of self-interacting modes $n - n$," *Phys. Rev. E* **101**, 013111 (2020).
- ²³C. Inserra, G. Regnault, S. Cleve, C. Mauger, and A. A. Doinikov, "Acoustic microstreaming produced by nonspherical oscillations of a gas bubble. IV. Case of modes n and m," *Phys. Rev. E* **102**, 043103 (2020).
- ²⁴R. H. Liu, J. Yang, M. Z. Pindera, M. Athavale, and P. Grodzinski, "Bubble-induced acoustic micromixing," *Lab Chip* **2**, 151–157 (2002).
- ²⁵P. Tho, R. Manasseh, and A. Ooi, "Cavitation microstreaming patterns in single and multiple bubble systems," *J. Fluid Mech.* **576**, 191–233 (2007).
- ²⁶S. Shklyaev and A. V. Straube, "Linear oscillations of a compressible hemispherical bubble on a solid substrate," *Phys. Fluids* **20**(5), 052102 (2008).
- ²⁷M. Fauconnier, J.-C. Béra, and C. Inserra, "Nonspherical modes nondegeneracy of a tethered bubble," *Phys. Rev. E* **102**, 033108 (2020).
- ²⁸S. Cleve, M. Guédra, C. Mauger, C. Inserra, and P. Blanc-Benon, "Microstreaming induced by acoustically trapped, non-spherically oscillating microbubbles," *J. Fluid Mech.* **875**, 597–621 (2019).
- ²⁹T. J. Asaki and P. L. Marston, "Free decay of shape oscillations of bubbles acoustically trapped in water and sea water," *J. Fluid Mech.* **300**, 149–167 (1995).
- ³⁰B. Saint-Michel and V. Garbin, "Acoustic bubble dynamics in a yield-stress fluid," *Soft Matter* **16**, 10405–10418 (2020).
- ³¹M. Versluis, D. E. Goertz, P. Palanchon, I. L. Heitman, S. M. van der Meer, B. Dollet, N. de Jong, and D. Lohse, "Microbubble shape oscillations excited through ultrasonic parametric driving," *Phys. Rev. E* **82**, 026321 (2010).
- ³²See supplementary material at <https://www.scitation.org/doi/suppl/10.1121/10.0005821> for MATLAB code for streaming predictions and videos of the bubbles on mode 3, mode 4, and induced flows.
- ³³R. Ben Haj Slama, B. Gilles, M. B. Chiekh, and J.-C. Béra, "PIV for the characterization of focused field induced acoustic streaming: Seeding particle choice evaluation," *Ultrasonics* **76**, 217–226 (2017).
- ³⁴J.-Y. Tinevez, N. Perry, J. Schindelin, G. M. Hoopes, G. D. Reynolds, E. Laplantine, S. Y. Bednarek, S. L. Shorte, and K. W. Eliceiri, "Trackmate: An open and extensible platform for single-particle tracking," *Methods* **115**, 80–90 (2017).
- ³⁵A. M. Soto, P. Penas, G. Lajoinie, D. Lohse, and D. van der Meer, "Ultrasound-enhanced mass transfer during single-bubble diffusive growth," *Phys. Rev. Fluids* **5**, 063605 (2020).
- ³⁶P. Marmottant and S. Hilgenfeldt, "Controlled vesicle deformation and lysis by single oscillating bubbles," *Nature* **423**, 153–156 (2003).
- ³⁷F. Mekki-Berrada, T. Combriat, P. Thibault, and P. Marmottant, "Interactions enhance the acoustic streaming around flattened microfluidic bubbles," *J. Fluid Mech.* **797**, 851–873 (2016).
- ³⁸A. Marin, M. Rossi, B. Rallabandi, C. Wang, S. Hilgenfeldt, and C. J. Kähler, "Three-dimensional phenomena in microbubble acoustic streaming," *Phys. Rev. Appl.* **3**, 041001 (2015).
- ³⁹F. Prabowo and C.-D. Ohl, "Surface oscillation and jetting from surface attached acoustic driven bubbles," *Ultrasonics Sonochem.* **18**(1), 431–435 (2011).
- ⁴⁰V. Pereno, M. Aron, O. Vince, C. Mannaris, A. Seth, M. de Saint Victor, G. Lajoinie, M. Versluis, C. Coussios, D. Carugo, and E. Stride, "Layered acoustofluidic resonators for the simultaneous optical and acoustic characterisation of cavitation dynamics, microstreaming, and biological effects," *Biomicrofluidics* **12**(3), 034109 (2018).
- ⁴¹A. van Wamel, K. Kooiman, M. Hartevelde, M. Emmer, F. J. ten Cate, M. Versluis, and N. de Jong, "Vibrating microbubbles poking individual cells: Drug transfer into cells via sonoporation," *J. Cont. Rel* **112**(2), 149–155 (2006).
- ⁴²S. A. Elder, "Cavitation microstreaming," *J. Acoust. Soc. Am.* **31**(1), 54–64 (1959).
- ⁴³M. Guédra and C. Inserra, "Bubble shape oscillations of finite amplitude," *J. Fluid Mech.* **857**, 681–703 (2018).
- ⁴⁴S. Roovers, T. Segers, G. Lajoinie, J. Deprez, M. Versluis, S. C. De Smedt, and I. Lentacker, "The role of ultrasound-driven microbubble dynamics in drug delivery: From microbubble fundamentals to clinical translation," *Langmuir* **35**(31), 10173–10191 (2019).
- ⁴⁵J. Collis, R. Manasseh, P. Liovic, P. Tho, A. Ooi, K. Petkovic-Duran, and Y. Zhu, "Cavitation microstreaming and stress fields created by microbubbles," *Ultrasonics* **50**(2), 273–279 (2010).
- ⁴⁶B. Dollet, S. M. van der Meer, V. Garbin, N. de Jong, D. Lohse, and M. Versluis, "Nonspherical oscillations of ultrasound contrast agent microbubbles," *Ultrasound Med. Biol.* **34**(9), 1465–1473 (2008).
- ⁴⁷W. Kim, T. H. Kim, J. Choi, and H. Y. Kim, "Mechanism of particle removal by megasonic waves," *Appl. Phys. Lett.* **94**, 081908 (2009).